



# Design and development of the beamline for a proton therapy system

Bin Qin<sup>1</sup> · Xu Liu<sup>1</sup> · Qu-Shan Chen<sup>1</sup> · Dong Li<sup>1</sup> · Wen-Jie Han<sup>1</sup> ·  
Ping Tan<sup>1</sup> · Zhong-Qi Zhang<sup>1</sup> · Chong Zhou<sup>1</sup> · Ao-Te Chen<sup>1</sup> · Yi-Cheng Liao<sup>1</sup> ·  
Wei Wang<sup>1</sup>

Received: 16 July 2021 / Revised: 14 October 2021 / Accepted: 25 October 2021 / Published online: 11 December 2021  
© The Author(s), under exclusive licence to China Science Publishing & Media Ltd. (Science Press), Shanghai Institute of Applied Physics, the Chinese Academy of Sciences, Chinese Nuclear Society 2021

**Abstract** A proton therapy (PT) facility with multiple treatment rooms based on the superconducting cyclotron scheme is under development at Huazhong University of Science and Technology (HUST). This paper attempts to describe the design considerations and implementation of the PT beamline from a systematic viewpoint. Design considerations covering beam optics and the influence of high-order aberrations, beam energy/intensity modulation, and beam orbit correction are described. In addition to the technical implementation of the main beamline components and subsystems, including the energy degrader, fast kicker, beamline magnets, beam diagnostic system, and beamline control system are introduced.

**Keywords** Proton therapy · Beamline · Beam optics · Beam energy/intensity modulation

## 1 Introduction

For a cyclotron-based proton therapy (PT) facility, the beamline is an important system that ‘optimally’ transports the proton beam from the point of extraction from the

accelerator to the treatment nozzle [1, 2]. In general, a PT beamline can be divided into several function sections, including an energy selection section that modulates the beam energy and intensity, beam switch and period sections that can deliver the beam to specific treatment rooms, and a fixed beamline (horizontal, vertical, or specific project angles)/gantry beamline that delivers the beam to the treatment nozzles. Because the rotating gantry is capable of bending a fixed horizontal proton beam in any direction perpendicular to the irradiation plane at the iso-center, it is a standard and essential configuration in modern PT facilities.

The main functions of the beamline before the gantry are as follows: (1) beam energy modulation using an energy degrader according to the treatment plan, and beam quality (beam emittance and momentum spread) recovery with downstream collimators and an energy slit; (2) beam switch/distribution to a specific treatment room following the command from the treatment control system (TCS); (3) optical matching of beam size and lattice function at some critical positions to maintain highly efficient beam transportation and minimum beam loss. The gantry beamline transports a ‘round’ beam from the coupling point, which is located at the entrance of the gantry, to the nozzle and iso-center. The variation in the beam size at the iso-center should be confined to within a limit for all beam energies and rotation angles.

A PT facility based on a superconducting cyclotron is under construction at Huazhong University of Science and Technology (HUST-PTF) [3, 4]. The overall layout is illustrated in Fig. 1, and the main specifications are listed in Table 1. In the beam transport line, an energy selection system (ESS) is capable of modulating the proton beam energy and intensity according to the requirements of

---

This work was supported by the National Key Research and Development Program of China (No. 2016YFC0105305), the National Natural Science Foundation of China (11975107), and the Program for HUST Academic Frontier Youth Team.

---

✉ Bin Qin  
bin.qin@mail.hust.edu.cn

<sup>1</sup> State Key Laboratory of Advanced Electromagnetic Engineering and Technology, School of Electrical and Electronic Engineering, Huazhong University of Science and Technology, Wuhan 430074, Hubei, China

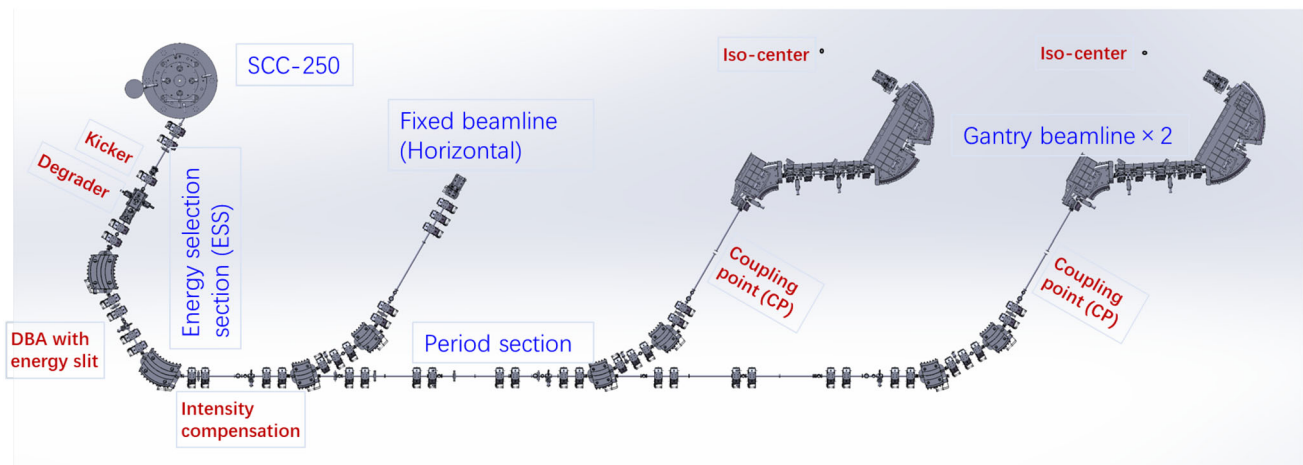


**Fig. 1** (Color online) Overall layout of HUST-PTF

**Table 1** Main specifications of HUST-PTF

Parameter	Specification
Accelerator type	Superconducting cyclotron
Energy range from ESS (MeV)	70–240
Gantry type	$\pm 180$ degrees, normal conducting
Scanning method	Downstream, pencil beam scanning (PBS)
Beam intensity at iso-center (nA)	0.4–5
Virtual SAD (m)	2.8
Field size (cm <sup>2</sup> )	30 × 30

clinical treatment. After the ESS, three identical switch sections can deliver the beam to one horizontal fixed beamline and two downstream 360° gantry beamlines. Each switch section uses a double-bend achromatic (DBA) lattice, which consists of two dipoles with 30° bending angles and seven quadrupoles.

## 2 Design considerations on beam optics

The beam optics of the HUST-PTF beamline was calculated and matched using the Transport code [5]. Figure 2 shows a  $2\sigma$  beam envelope from the cyclotron exit to the iso-center of the first gantry. From previous experiences, the linear beam optics calculated by the Transport code will match well, especially when the momentum dispersion is small (e.g.,  $\Delta p/p = \pm 0.6\%$ ) and cross-talk effects between beamline magnets are not dominant. However, in order to investigate high-order aberrations and the influence of fringe fields on beam optics, we used COSY Infinity [6] and OPERA-3D [7] for validating the beam behavior in realistic situations.

### 2.1 Modulation of beam energy and intensity

For cyclotron-based PT, one drawback is the fixed beam energy extracted from the accelerator. To deliver various energy proton beams for different deposit depths, an ESS that consists of an energy degrader and a downstream DBA section with an energy slit is required.

To precisely evaluate beam transmission in an ESS, the Monte Carlo code Geant4 [8] with the capability to simulate beam-material interactions is applied. Detailed works can be found in [9]. Owing to multiple Coulomb scatterings in the carbon material during energy degradation, the beam quality in terms of the energy spread and the beam emittance deteriorates and needs to be recovered by collimators located downstream of the degrader wedge and an energy slit located at the center of the DBA. The beam loss due to this recovery process will lead to a significant difference in the transmission of the beam energy in the range of 70–230 MeV. As shown in Fig. 4, the overall transmission was below 0.1% for 70 MeV and 14% for 230 MeV. However, it should be noted that minor disagreements regarding the beam transmission exist between the Monte Carlo simulation and the measured data [10], and corrections should be made based on experimental studies.

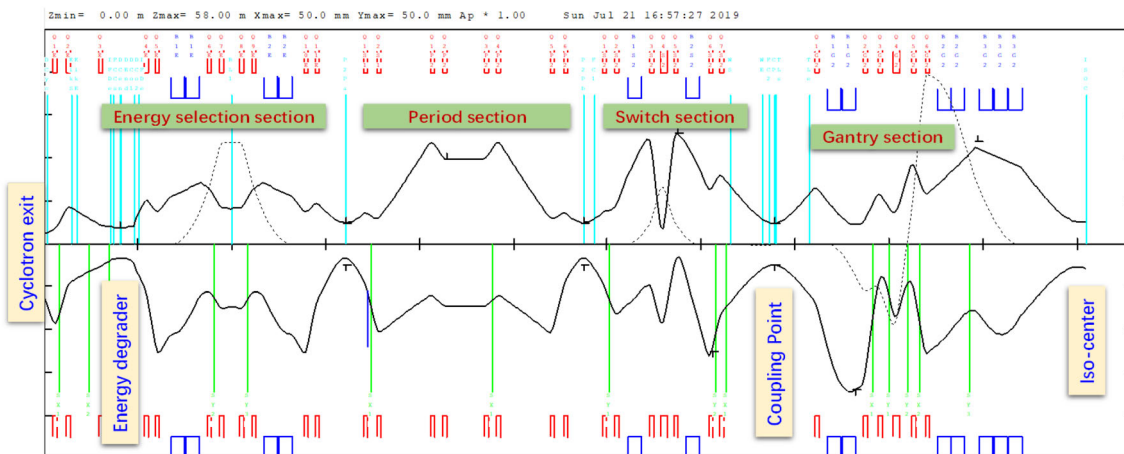


**Fig. 2** (Color online)  $2\sigma$  beam ( $\epsilon_{x,y} = 28\pi \text{ mm} \cdot \text{mrad}$ ,  $\Delta p/p = \pm 0.6\%$ ) envelope from the exit of the cyclotron to the iso-center of the first gantry, calculated and fitted by the Transport code

An investigation was performed to determine the natural intensity configuration of a proton beam so that it could be matched to the calculated overall transmission. We used the Geant4 code to simulate the dose rate in one liter of water: each energy plane was set to an area of  $100 \text{ mm} \times 100 \text{ mm}$  with a  $5 \text{ mm}$  spot interval. For a  $100 \text{ mm}$  depth axis, it contained 21 energy layers in intervals of  $5 \text{ mm}$ . The total beam switch time for one energy layer is estimated to be  $690 \text{ ms}$ , which includes a  $250 \text{ ms}$  energy switch time and  $440 \text{ ms}$  of switch time for spot scanning ( $2 \text{ ms}$  for line switch, and  $1 \text{ ms}$  for spot switch). The overall transmission shown in Fig. 4 was applied to calculate the beam intensity for each energy layer. As an example, for a SOBP  $230\text{--}330 \text{ mm}$  (corresponding to  $186.6 \text{ MeV} - 230 \text{ MeV}$ ), a dose rate of  $6.86 \text{ Gy/min/L}$  can be achieved when beam intensity is  $4 \text{ nA}$  at  $230 \text{ MeV}$ . With this method, the relationship between the dose rate and the maximum beam intensity at the far end of the SOBP can be established.

By using these data, and to overcome the large variance in beam transmission across the total energy range, we developed an intensity modulation strategy for the extracted proton beam of the isochronous cyclotron by adjusting the inflector voltage in the central region. As shown in Fig. 5, three settings were applied:  $220 \text{ nA}$  for  $70\text{--}170 \text{ MeV}$ ,  $80 \text{ nA}$  for  $170\text{--}210 \text{ MeV}$ , and  $35 \text{ nA}$  for energies higher than  $210 \text{ MeV}$ . With this setup, a minimum dose rate of  $2.61 \text{ Gy/min/L}$  at the shallow SOBP ( $42\text{--}142 \text{ mm}$ ,  $70\text{--}141 \text{ MeV}$ ) and a maximum dose rate of  $8.36 \text{ Gy/min/L}$  at SOBP ( $230\text{--}330 \text{ mm}$ ) could be achieved.

The system also provides a beam intensity suppression method for achieving a smooth and continuous beam intensity across the full energy range. As shown in Fig. 3, when the beam intensity in the higher energy region exceeds the limit, two quadrupoles, Q10E and Q11E after B2E, will be tuned to ‘defocus’ the beam and cut off some

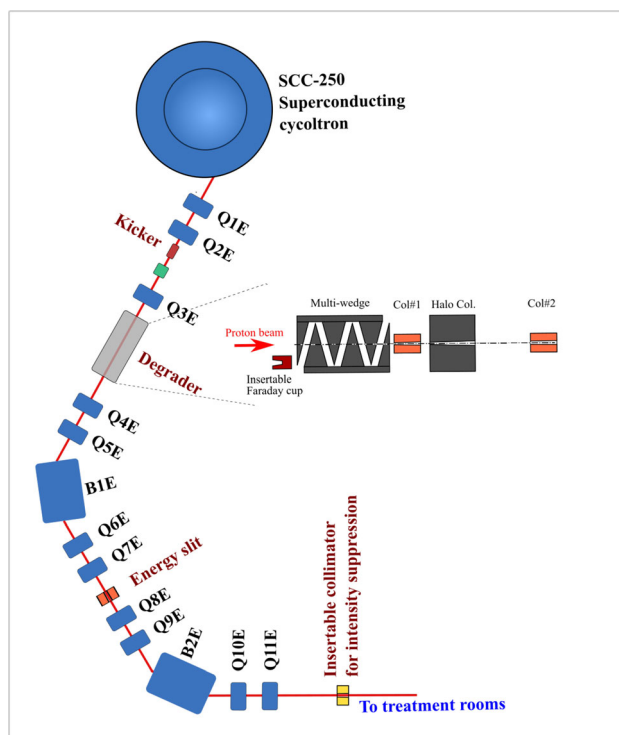


**Fig. 3** (Color online) Layout of the ESS

portion of the beam. A detailed implementation can be found in Ref. [11]. This technique was first applied to the PSI gantry 3 [12].

We reserve this beam intensity suppression method as a backup mechanism for when the extracted beam intensity is constant during operation. However, when applying this method, the beam emittance will decrease significantly for a defocused high-energy beam, which will increase the complexity of the treatment plan. Additionally, the extra

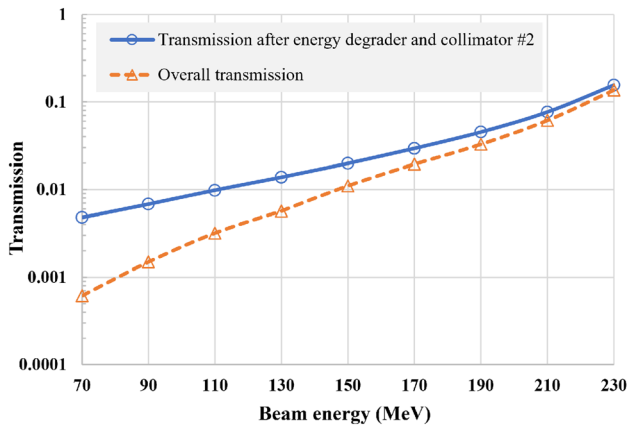


**Fig. 4** (Color online) Beam transmission after the energy degrader and collimator #2 (solid line), and overall transmission after the energy slit of DBA with momentum selection of  $\Delta p/p = \pm 0.6\%$  + 10% beam loss in the downstream beamline (dashed line)

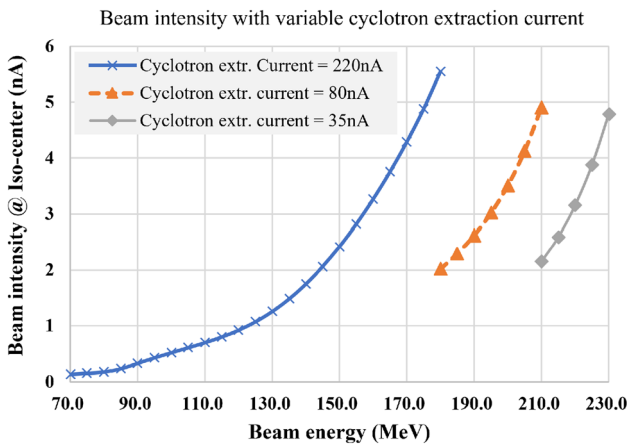


**Fig. 5** (Color online) Three stage intensity modulation with variable cyclotron extraction current for final treatment

focusing strength adjustment of Q10E and Q11E will also increase the beamline complexity and uncertainties.

### 2.2 Influence of high order aberrations and fringe fields on gantry beamline

For the downstream scanning gantry beamline, image optics is applied to achieve a 1:1 magnification factor between the entrance coupling point and the iso-center. It consists of five regular quadrupoles, one long quadrupole, two dipoles with a bending angle of  $57^\circ$ , and a bending angle of  $90^\circ$ . The design details can be found in Ref. [4].

Considering the sensitivity and stability requirements of the rotation gantry beamline, a more sophisticated study on beam optics beyond the linear optics results calculated by the Transport code should be performed. We used Cosy Infinity to investigate the influence of high-order

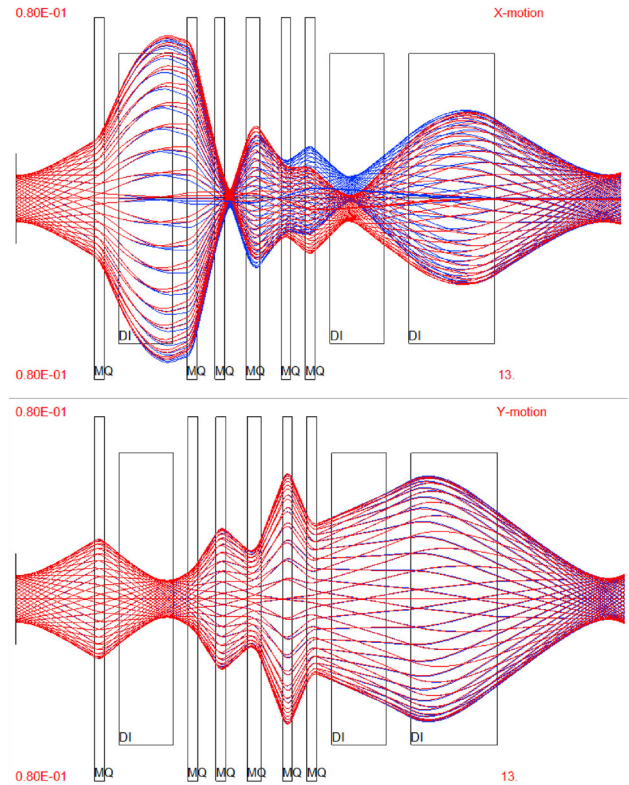


**Fig. 6** (Color online) Multi-particle ray-tracing of beam trajectory in the gantry beamline, using fifth order optics in Cosy Infinity: (top) X (dispersive) plane motion; (bottom) Y (non-dispersive) plane motion. The blue lines represent  $\Delta p/p = +0.6\%$ , and the red lines represent  $\Delta p/p = -0.6\%$  protons with an energy of 230 MeV. (Color figure online)

aberrations and fringe magnetic fields on the beam optics and beam profiles [13].

The Enge function [14] is used to fit the realistic fringe fields of all gantry beamline magnets to coefficients that can be input into Cosy Infinity with the fringe field mode FR 2.5. The fitted beam optics from the Transport code are used as a baseline for Cosy Infinity, but the field gradients of all six quadrupoles were re-fitted using the realistic Enge coefficients. For the optimized optics parameters, there are minor adjustments for the quadrupole strength compared with the baseline parameters, with a maximum deviation of  $\pm 8\%$ . The multi-particle ray-tracing results up to the fifth order are illustrated in Fig. 6. The beam size at the iso-center was well-controlled for a momentum dispersion of  $\pm 0.6\%$ .

### 2.3 Beam orbit simulation and correction

Beam orbit correction is an indispensable procedure in accelerator commissioning and operation. A beamline usually contains various errors due to issues in the manufacture and installation of the magnets, with the primary

**Table 2** Error settings in the simulation

Fixed beamline		
Component	Error item	Amplitude
Quadrupole	Offset ( $\Delta x, \Delta y, \Delta s$ )	$\pm 0.2$ mm
Quadrupole	Tilt ( $\Delta\theta_s$ )	$\pm 0.5$ mrad
Quadrupole	Field	0.1 %
Dipole	Offset ( $\Delta x, \Delta y, \Delta s$ )	$\pm 0.2$ mm
Dipole	Tilt ( $\Delta\theta_s$ )	$\pm 0.5$ mrad
Dipole	Field	$\pm 0.1$ %
Gantry Beamline		
Component	Error item	Amplitude
Quadrupole	Offset ( $\Delta x, \Delta y, \Delta s$ )	$\pm 0.4$ mm
Quadrupole	Tilt ( $\Delta\theta_s$ )	$\pm 1.0$ mrad
Quadrupole	Field	$\pm 0.1$ %
Dipole	Offset ( $\Delta x, \Delta y, \Delta s$ )	$\pm 0.4$ mm
Dipole	Tilt ( $\Delta\theta_s$ )	$\pm 1.0$ mrad
Dipole	Field	$\pm 0.1$ %
Gantry	Main frame offset ( $\Delta x, \Delta y$ )	$\pm 0.2$ mm
Fixed+Gantry Beamline		
Component	Error item	Amplitude
BPM	Offset ( $\Delta x, \Delta y$ )	$\pm 0.25$ mm
BPM	Tilt ( $\Delta\theta_s$ )	$\pm 2$ mrad
Steerer	Tilt ( $\Delta\theta_s$ )	$\pm 2$ mrad

contributions coming from misalignments and field perturbations. These errors lead to a deviation in the beam trajectory from the design orbit and influence the beam quality. For a PT facility, the maximum beam offset at the treatment terminal must be controlled to within  $\pm 1$  mm according to the clinical treatment criteria. To accurately evaluate the beam orbit deviation, we performed a simulation using the ELEGANT code [16] and added the following error terms to the simulation, as listed in Table 2.

Using the beamline to the first gantry room in the HUST-PTF as an example, the beam orbit deviation is presented in Fig. 7). The maximum root-mean-square (RMS) value is approximately 25 mm in the horizontal direction and 17 mm in the vertical direction, which is unacceptable for beam transmission. We adopted the response matrix method and placed a series of steerer magnets to correct the beam orbit. The correction strategy is global correction, which simultaneously minimizes the beam offset at the iso-center and along the beamline. To achieve the optimal correction effect, all candidate positions for placing steerers were numbered, and the best layout was determined using a genetic algorithm [15]. With the optimal configuration of steerers, the orbit deviation can be reduced to less than 2 mm (RMS value), and the maximum beam offset at the iso-center is limited to 0.3 mm.

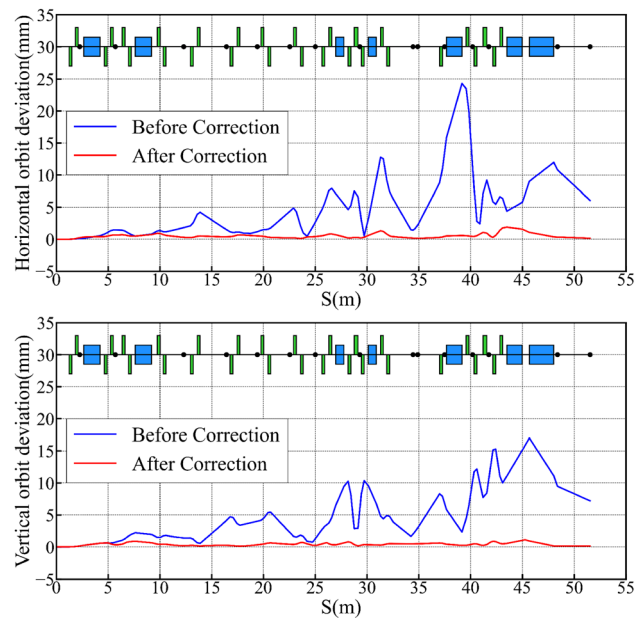


**Fig. 7** (Color online) RMS value of the beam orbit deviation before and after correction from the exit of the degrader to the iso-center in the first gantry room. The lattice structure is plotted at the top: the quadrupole and dipole magnets are colored green and blue, respectively, and the black dot indicates the position of the BPM. (Color figure online)

### 3 Features of beamline elements

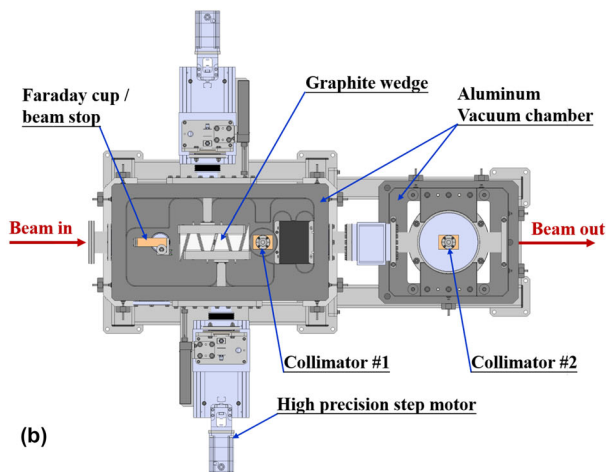
#### 3.1 Multi-wedge energy degrader

To realize continuous and fast beam energy modulation, a multi-wedge-style degrader was adopted. High-density isotropic graphite was chosen for the degrader material considering the relatively lower Z and easy machining of the wedge shape. The main tested parameters of graphite are listed in Table 3). Figure 8 a shows one machined and processed graphite wedge unit, with wedge number 2.5 and a wedge angle of  $30^\circ$ .

Figure 8 b shows the uncovered structural top view of the degrader system. The vacuum chamber is made of aluminum to minimize the activation level during the energy degradation process. Inside the main vacuum chamber, a Faraday cup is placed upstream of the graphite wedge pair. The nominal center position of the Faraday cup is 18 mm offset with respect to the beam axis in the vertical direction in order to receive the proton beam deflected by a fast kicker magnet upstream and fulfill both functions of beam dump and intensity measurement. In the emergency status, this Faraday cup can be driven to the beam axis by a pneumatic actuator for beam safety, with an action time of less than 1 s. Downstream of the graphite wedge, two collimators (Col. #1, Col. #2) are installed to ‘re-define’ the rms beam emittance to the selected values of  $5\pi/7\pi/10\pi$  mm · mrad. The degrader has been

**Table 3** Tested parameters of the graphite

Parameter	Specification
Volume density ( $\text{g}/\text{cm}^3$ )	1.95
Purity (%)	99.997
Degree of isotropy	1.046
Thermal expansion coefficient (at $25^\circ\text{C}$ )	$6.75 \times 10^{-6}/\text{K}$
Bending strength (MPa)	66.8
Compressive strength (MPa)	152.0

**Fig. 8** (Color online) **a** One machined graphite wedge unit; **b** Uncovered structural model of the multi-wedge energy degrader

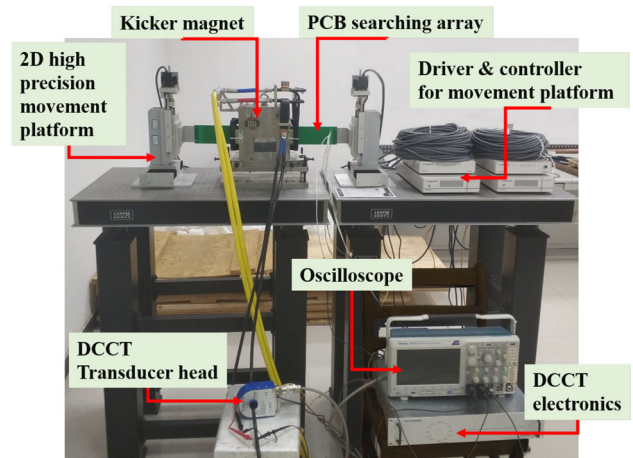
manufactured and tested without a beam load. The positioning errors of the graphite wedge and the collimators are less than  $10 \mu\text{m}$ , and the wedge movement time corresponding to a single energy layer is less than 200 ms.

### 3.2 Kicker for fast beam switch

For the purpose of fast ON/OFF beam switching during an energy layer change and lateral spot scanning, a fast

**Table 4** Main specifications of the kicker magnet

Parameter	Specification
Integral magnetic field ( $\text{T} \cdot \text{mm}$ )	25.2
Magnet length (mm)	300
Magnet aperture ( $H \times V$ ) ( $\text{mm}^2$ )	$50 \times 82$
Good field region (GFR) (mm)	$\pm 12 (H) / \pm 30 (V)$
Field homogeneity in GFR	$\leq \pm 0.5\%$
Rise/fall time	$< 100 \mu\text{s}$

**Fig. 9** (Color online) Dynamic magnetic field measurement platform based on PCB technique

kicker magnet will be installed upstream of the energy degrader. The switch time is required to be less than  $100 \mu\text{s}$ , and the maximum repetition rate should be up to 500 Hz. The main specifications of the kicker magnet are listed in Table 4. The design, fabrication, and testing of this fast kicker magnet and the associated pulsed power supply have been accomplished [17, 18]. For a specific design of the pulsed power supply, the kicker magnet can also be operated in the long-term DC mode, adhering to safety requirements by deflecting the beam to the downstream Faraday cup for a time duration longer than 5 s.

To obtain the dynamic response feature of the magnetic field, a measurement system based on a printed circuit board (PCB) searching coil array scheme was developed [19], as shown in Fig. 9). Figure 10 shows the measured result of the dynamic magnetic field, which is approximately  $63 \mu\text{s}$ . The integral magnetic field can reach  $25.2 \text{ T} \cdot \text{mm}$  with an excitation current of 510 A, which fulfills the design specifications.

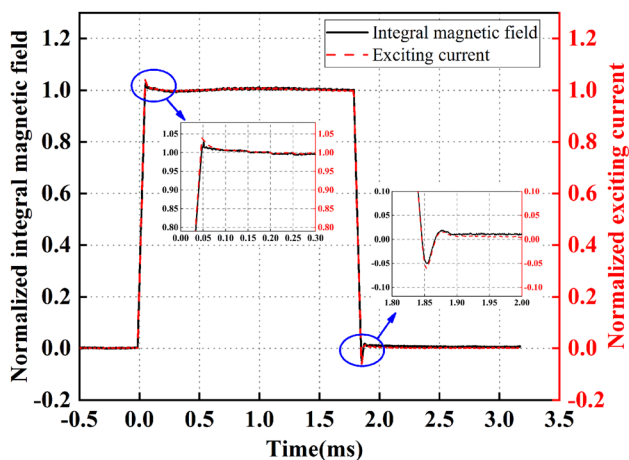


**Fig. 10** (Color online) Measured dynamic response and lag effect of the integral magnetic fields

### 3.3 Tapered scanning magnet

A pencil beam scanning (PBS) nozzle with two mutually perpendicular dipole magnets is applied to deflect the proton beam and form a radiation field that is conformal with the tumor. To effectively reduce the required excitation current while accommodating the envelope of the scanning proton beam, the pole gap of the second magnet SMX was designed to be tapered from 110 mm to 72 mm, while the pole gap of the SMY was kept constant at 60 mm. The design details can be found in Ref. [20].

For a verification of the performance of the tapered scanning magnet, beam tracking was performed to simulate the behavior of the beam in the PBS nozzle. Figure 11 a shows the tapered SMX model. Because the field size is 30 cm × 30 cm, a maximum offset of 15 cm for a 70 MeV proton beam at the iso-center was simulated. Figures 11 b and c show the beam spot at the entrance of the nozzle and at the iso-center, respectively. The variations in beam size and center of the beam spot are less than 0.1 mm compared with those using a constant 110 mm pole gap, while the excitation current could be reduced from 276.8 A to 228.2 A.

### 3.4 Beamline magnets

The beamline contains 59 quadrupoles, 14 dipoles, and 31 correctors. The main specifications are listed in Table 5. All magnets, excluding those at the second gantry beamline, were manufactured, and the magnetic field quality fulfilled the specifications. Figure 12 shows the measured results of the regular quadrupoles, with three operation currents ranging from 10% to 100%. The sextupole components ( $n = 3$ ) and other main multipole errors ( $n = 4, 6, 10$ ) were measured and controlled to within five

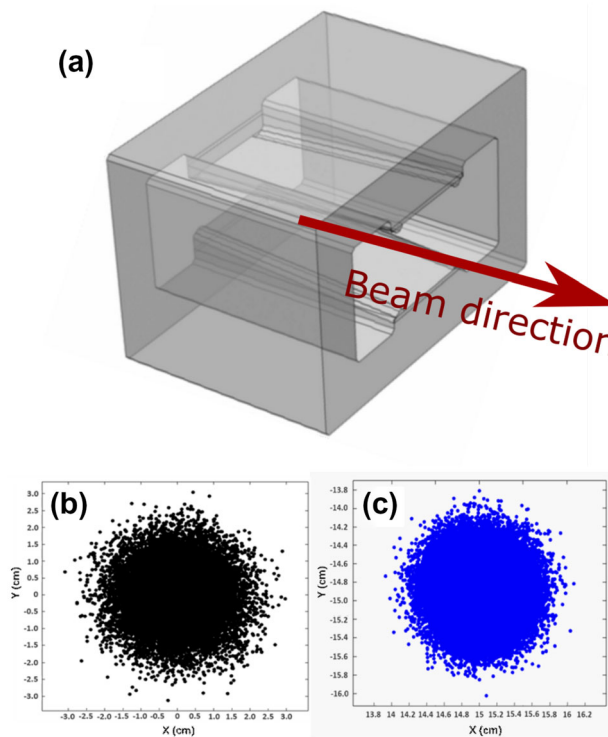


**Fig. 11** (Color online) **a** Tapered SMX scanning magnet model; **b** 70 MeV beam profile at the entrance of the nozzle; **c** 70 MeV beam profile at the iso-center

units. Figure 13 shows the measured integral field homogeneity of two 57° dipoles and one 90° dipole affiliated with the first gantry beamline, with operation currents of 245 A and 501 A for central magnetic fields of 0.82 T and 1.62 T, respectively. A field homogeneity of  $\pm 0.03\%$  at the mid-plane corresponding to a magnetic field range of 50% and 100% was achieved. All dipoles and quadrupoles have a relatively good linearity in terms of field excitations.

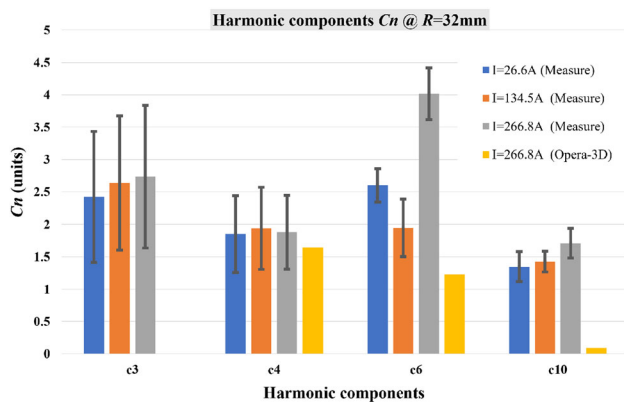
## 4 Beam diagnostics and beamline control

### 4.1 Beam diagnostic system

The beam diagnostic system (BDS) is essential for beam commissioning and routine operation. The main purposes of the BDS are (1) beam intensity measurements, (2) beam position measurements for orbit correction, and (3) beam profile measurements for optics studies. Owing to the ultra-low intensity beam current downstream of the ESS, it would be very challenging to use an inductive or non-destructive detector and obtain an effective signal. As a compromise between cost and effectiveness there are three types of commonly used detectors, a scintillation screen (SC), an ionization chamber (IC), and a Faraday cup

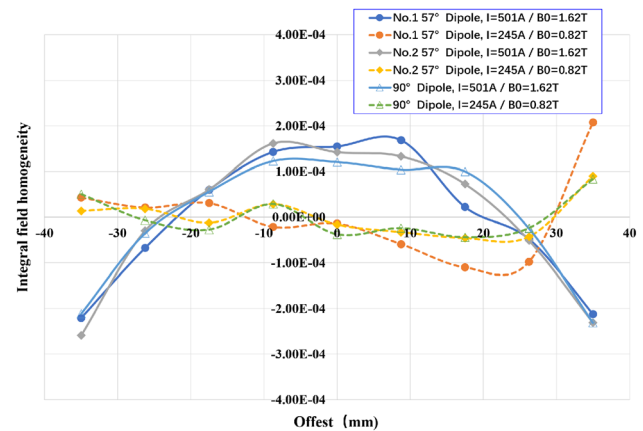
**Table 5** Specifications for beamline magnets

Magnet	Specification	Value
Quadrupoles (all types)	Aperture (mm)	80
	Max. field gradient (T/m)	18.0
	Integral field harmonics error	$\leq 5$ units
Regular quadrupole	Effective length (mm)	270
	Quantity	54
Long quadrupole	Effective length (mm)	370
	Quantity	5
Dipoles (all types)	Bending radius (mm)	1500
	Central magnetic field (T)	0.82–1.62
	Integral field homogeneity	$\leq \pm 0.08\%$
30° Dipole for fixed beamline	Entrance/exit edge angle (°)	15 / 15
	Quantity	6
60° Dipole for fixed beamline	Entrance/exit edge angle (°)	30 / 30
	Quantity	2
57° Dipole for gantry beamline	Entrance/exit edge angle (°)	0 / 0
	Quantity	4
90° Dipole for gantry beamline	Entrance/exit edge angle (°)	25 / 16.6
	Quantity	2
Steerers	Type	Separating ( <i>X</i> or <i>Y</i> direction)
	Overall length (mm)	$\leq 120$
	Max. integral field (T·mm)	12.2
	Quantity of	16 ( <i>X</i> -direction), 15 ( <i>Y</i> -direction)

**Fig. 12** (Color online) Measured multipole components ( $n \geq 3$ ) of regular quadrupoles at operation currents of 26.3 A (1.8 T/m), 134.5 A (9.3 T/m) and 266.8 A (18.0 T/m)

(FC). Figure 14 shows the SC, FC and thick IC of HUST-PTF.

One FC is installed at the entrance of the energy degrader for beam collection during ‘Kicker ON’ and it is the only one equipped with water cooling. The others are installed downstream of the ESS to measure the beam intensity, as well as the beam stop in emergency cases. The cup was made of oxygen-free copper. An electrode with a bias voltage of  $-100$  V was placed at the entrance of the cup to repel secondary electrons. The entire structure was

**Fig. 13** (Color online) Measured integral field homogeneity of two 57° dipoles and one 90° dipole affiliated with the first gantry beamline at operation currents of 245 A and 501 A for central magnetic fields of 0.82 T and 1.62 T, respectively

optimized to ensure that more than 98% of the protons and secondary particles could be collected by the cup.

The beam position and profile were measured by the SCs and ICs. The SCs were installed in the fixed beamlines, while thick ICs were installed in the gantry beamlines. The main consideration behind this deployment is that it is easier to maintain and replace the CCD camera of the SC in fixed beamlines than in the gantry beamlines. The screen material of the SC is  $\text{Al}_2\text{O}_3:\text{Cr}$ , designed by the Institute of

**Table 6** Detectors and their numbers used in the beamline

Detectors	Number	Retractable
FC (w. water cooling)	1	Yes
FC (w.o. water cooling)	6	Yes
SC	20	Yes
Thin IC	3	No
Thick IC	6	Yes

Modern Physics, Chinese Academy of Sciences. Offline tests showed that the optical resolution of the SC was 0.08 mm/pixel. The thick IC has a double-stack configuration and can simultaneously measure the horizontal and vertical distributions. The chamber used clean dry air at standard atmospheric temperature and pressure, and the highest anode voltage was 2 kV.

Apart from the retractable detectors, there are three fixed and thin ICs (IC64-6 from Pyramid Technical Consultants Inc.) installed in the air gaps before each treatment room for online beam monitoring. They can provide an interlock signal to the machine control system when an abnormal signal is detected. The numbers of each type of detector are summarized in Table 6. For security considerations, all retractable detectors are set to be pushed in when the pneumatic actuator is powered off and pulled out when the actuator is powered on. A prototype of each type of detector was manufactured and tested. More detailed design and testing results of the BDS can be found in Ref. [21].

#### 4.2 Beamline control system

The beamline control system (BCS) is the ‘core’ of the beamline with the following major functions: (1) Full control access and management to all low-level hardware modules of the beamline, which includes the power supplies of all dipoles, quadrupoles, steerers, kicker, energy degrader, and beam diagnostic modules; (2) mode switch between beam commissioning and routine beam treatment; (3) to provide a fast response and data exchange interface for external software components of PT, such as the treatment control system (TCS); (4) to provide a unified and friendly user interface (UI) for operators; and (5) data acquisition, logging, and supervision during beam commissioning and treatment procedures.

As shown in Fig. 15, the BCS adopts the OPC UA framework to ensure high safety and reliability and consists of three layers: a device layer, a server layer, and a GUI layer. To unify the communication protocol, special OPC UA servers are developed for each category of device,



**Fig. 14** (Color online) SC, FC and thick IC of HUST-PTF. All detectors are driven by pneumatic actuators

which act as a gateway to the server layer. In the server layer, the configuration service provides the actual operation parameters for devices from the database, for example, the currents for the magnet power supplies. The responsibility of the operation service is to direct the flow of the operations of the entire BCS. Each manager is in charge of an actual control of the corresponding devices.

To date, BCS has completed an operation workflow test based on a virtual simulation platform. BCS can achieve parallel monitoring of the subsystem status up to 1500 Hz, which meets the energy switching requirements.

#### 5 Discussion and conclusions

Compared with accelerator and beamline facilities used in scientific research, the main task of a PT beamline is to deliver a stable proton beam at a fixed treatment position or rotating gantry iso-center, to fulfill the requirements of treatment plans with acceptable deviations in beam size, intensity, and energy. Design considerations and technical implementations of the HUST-PTF beamline are reviewed from a systematic viewpoint, and some details can be found in the published literature.

The HUST-PTF beamline will be installed this year. For more efficient beam commissioning and precise dose delivery, the following studies will be performed:

1. From our experiences in gantry beamline modeling, the beam behavior differs between a linear optics model and a realistic model considering high order aberrations and fringe fields. To provide a more accurate prediction of the beam transportation, it is essential to build a high-fidelity beamline model from start to end, including beam material interactions with beam loss evaluation, and nonlinear effects using high-

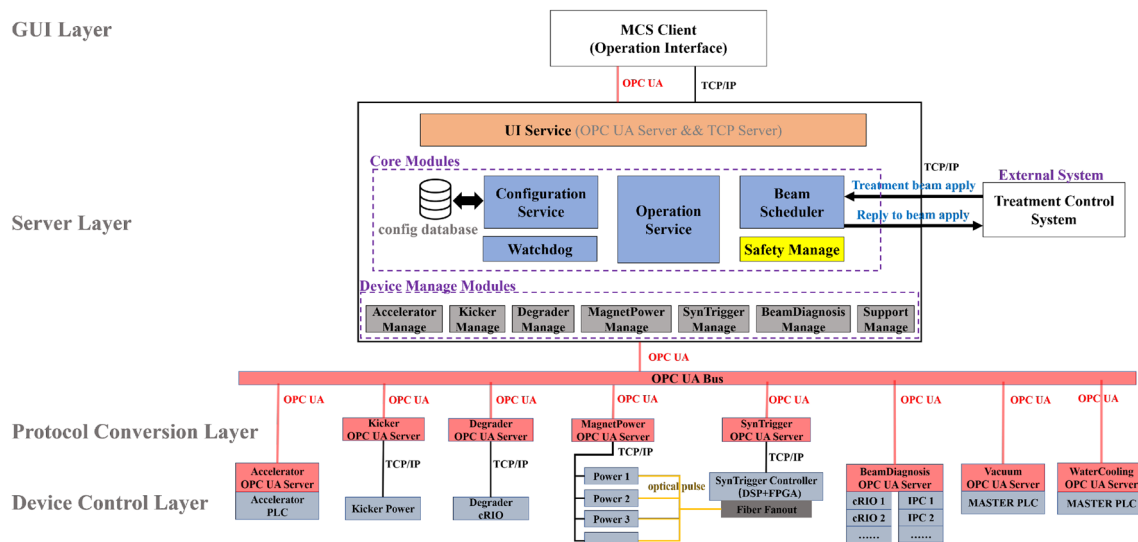


**Fig. 15** (Color online) Framework of BCS

order optics calculations or particle tracking in realistic magnetic fields. Related works have recently been initiated and studied in PSI and IBA [22, 23].

- For an important potential application, by training the pre-constructed high fidelity beamline model with machine learning algorithms such as neural networks, it is possible to construct more efficient surrogate models which can be embedded into the BCS to perform beam parameter prediction, correction and commissioning with an almost ‘real-time’ response performance.

**Acknowledgements** The authors would like to acknowledge Li-Zhen Ma, Qing-Gao Yao, and Wenjie Yang at IMP (CAS, China) and Chang-Dong Deng and Yu-Wen Wu at IHEP (CAS, China) for their support and fruitful discussions related to the design and field measurements of prototype magnets. In addition, we would like to thank Rui-Shi Mao and his team at IMP (CAS, China) for their help and contributions to the construction of the beam diagnostic system. We would also like to acknowledge Marco Schippers at PSI and Luciano Calabretta at INFN for their valuable suggestions and comments on this project.

**Author Contributions** All authors contributed to the study conception and design. Material preparation, data collection and analysis were performed by Bin Qin, Xu Liu, Qu-Shan Chen, Dong Li, Wen-Jie Han, Ping Tan, Zhongqi Zhang, Chong Zhou, Ao-Te Chen, Yi-Cheng Liao and Wei Wang. The first draft of the manuscript was written by Bin Qin and all authors commented on previous versions of the manuscript. All authors read and approved the final manuscript.

## References

- E. Pedroni, D. Meer, C. Bula et al., Pencil beam characteristics of the next-generation proton scanning gantry of PSI: design issues and initial commissioning results. *Eur. Phys. J. Plus* **126**, 66 (2011). <https://doi.org/10.1140/epjp/i2011-11066-0>
- J.M. Schippers, Beam-transport systems for particle therapy, CERN yellow reports: school proceedings, Vol. 1, CERN-2017-004-SP, p. 241, <https://doi.org/10.23730/CYRSP-2017-001.241>
- B. Qin, W. J. Han, X. Liu et al., Design and development of the beamline system for a proton therapy facility, In: Proceedings of IPAC2019, Melbourne, Australia, (2019), THPMP017
- B. Qin, W. Chen, X. Liu et al., Design of Gantry beamline for HUST proton therapy facility. *IEEE Trans. on Appl. Supercond.* **28**, 4400205 (2018). <https://doi.org/10.1109/TASC.2017.2772868>
- U. Rohrer, PSI graphic transport framework, based on a CERN-SLAC-FERMILAB version by K. L. Brown et al., (2007), [http://aea.web.psi.ch/Urs\\_Rohrer/MyWeb/trans.htm](http://aea.web.psi.ch/Urs_Rohrer/MyWeb/trans.htm)
- M. Berz, K. Makino, COSY INFINITY 10.0 Beam Physics Manual, (2017)
- Opera-3D reference, <http://www.operafea.com>
- J. Allison, K. Amako, J. Apostolakis et al., Recent developments in Geant4. *Nucl. Instrum. Meth. A* **835**, 186–225 (2016). <https://doi.org/10.1016/j.nima.2016.06.125>
- Z. Liang, K. Liu, B. Qin et al., Design and optimization of an energy degrader with a multi-wedge scheme based on Geant4. *Nucl. Instrum. Meth. A* **890**, 112–118 (2018). <https://doi.org/10.1016/j.nima.2018.01.073>
- F. Jiang, Y.T. Song, J.X. Zheng et al., Energy loss of degrader in SC200 proton therapy facility. *Nucl. Sci. Tech.* **30**, 4 (2019). <https://doi.org/10.1007/s41365-018-0526-6>
- W. Chen, J. Yang, B. Qin et al., Transmission calculation and intensity suppression for a proton therapy system. *Nucl. Instrum. Meth. A* **881**, 82–87 (2018). <https://doi.org/10.1016/j.nima.2017.10.047>
- A. Koschik et al., Gantry 3: Further development of the PSI PROSCAN Proton Therapy Facility, Proceedings of 6th IPAC, Richmond (USA), (2015)
- Z.F. Zhao, B. Qin, X. Liu et al., Influence of fringing field and second-order aberrations on proton therapy gantry beamline. *Nucl. Instrum. Meth. A* **940**, 479–485 (2019). <https://doi.org/10.1016/j.nima.2019.06.057>
- H.A. Enge, Effect of extended fringing fields on ion-focusing properties of deflecting magnets. *Rev. Sci. Instrum.* **35**, 278–287 (1964). <https://doi.org/10.1063/1.1718806>

15. X. Liu, Q.S. Chen, Y.C. Liao et al., Layout optimization of corrector magnets for a proton therapy beamline via genetic algorithm. *Nucl. Instrum. Meth. A* **982**, 164560 (2020). <https://doi.org/10.1016/j.nima.2020.164560>
16. M. Borland, ELEGANT: A flexible SDDS-compliant code for accelerator simulation, in *Advanced Photon Source LS-287*, (2000)
17. W. Han, X. Liu, B. Qin et al., Design considerations of a fast kicker system applied in a proton therapy beamline. *Nucl. Instrum. Meth. A* **940**, 199–205 (2019). <https://doi.org/10.1016/j.nima.2019.06.034>
18. W. Han, G.Q. Li, B. Qin et al., Development and measurement of a fast kicker magnet applied to a proton therapy facility. *Nucl. Instrum. Meth. A* **971**, 164094 (2020). <https://doi.org/10.1016/j.nima.2020.164094>
19. G.Q. Li, W. Han, B. Qin et al., Dynamic magnetic measurements of a Kicker magnet for a proton therapy facility. *Nuclear Techniques*, 43, 010201 (2020). <https://doi.org/10.11889/j.0253-3219.2020.hjs.43.010201> (in Chinese)
20. Z.Q. Zhang, P. Tan, X.Y. Li et al., Structural optimization of fast-scanning magnets for proton therapy devices. *IEEE Trans. Appl. Supercond.* **30**(4), 4401604 (2020). <https://doi.org/10.1109/TASC.2020.2981029>
21. A.T. Chen, Q.S. Chen, X. Liu et al., Prototype development of the beam diagnostic system of a proton therapy facility based on a superconducting cyclotron. *Nucl. Instrum. Meth. A* **998**, 165208 (2021). <https://doi.org/10.1016/j.nima.2021.165208>
22. V. Rizzoglio, A. Adelman, A. Gerbershagen et al., Uncertainty quantification analysis and optimization for proton therapy beam lines. *Physica Medica* **75**, 11–18 (2020). <https://doi.org/10.1016/j.ejmp.2020.05.013>
23. C. Hernalsteens, R. Tesse, S.T. Boogert et al., A novel approach to seamless simulations of compact hadro therapy systems for self-consistent evaluation of dosimetric and radiation protection quantities. *Europhys. Lett.* **132**, 50004 (2020). <https://doi.org/10.1209/0295-5075/132/50004>